

**Mo-99 2015 TOPICAL MEETING ON
MOLYBDENUM-99 TECHNOLOGICAL DEVELOPMENT**

**AUGUST 31-SEPTEMBER 3, 2015
HILTON BOSTON BACK BAY
BOSTON, MASSACHUSETTS**

**Generation of Gas Bubbles in a Fissioning Uranyl Sulfate Solution
Using an Electron Beam Linac**

T.A. Heltemes, S.D. Chemerisov, R. Gromov, V. Makarashvili, Z. Sun, K.E. Wardle,
J.L. Bailey, D.C. Stepinski, J.L. Jerden, M. Basavarajappa, and G.F. Vandegrift
Nuclear Engineering Division
Argonne National Laboratory, 9700 South Cass Avenue, Argonne, IL – US

ABSTRACT

In support of the development of accelerator-driven production of fission product Mo-99 as proposed by SHINE Medical Technologies, a 35 MeV electron linac was used to irradiate depleted-uranium (DU) uranyl sulfate dissolved in pH 1 sulfuric acid at average power densities of 6 kW, 12 kW, and 15 kW. During these irradiations, gas bubbles were generated in solution due to the radiolytic decomposition of water molecules in the solution. Multiple video cameras were used to record the behavior of bubble generation and transport in the solution. Seven six-channel thermocouples were used to record temperature gradients in the solution from self-heating. Measurements of hydrogen and oxygen concentrations in a helium sweep gas were recorded by a gas chromatograph to estimate production rates during irradiation. These data are being used to validate a computational fluid dynamics (CFD) model of the experiment that includes multiphase flow and a custom bubble injection model for the solution region.

1. Introduction

SHINE Medical Technologies is planning to use neutron-induced fission in a subcritical low-enriched-uranium uranyl-sulfate target solution for production of ^{99}Mo [1,2]. During operation, the solution will undergo self-heating due to fissioning in the solution, radiolytic decomposition of the water in the solution, and circulation due to thermal gradients generated in the solution, which is cooled by cooling tubes running through the annulus and from cooling outside the annulus. Because formation of the radiolysis-induced bubbles (H_2 and O_2) their size and dynamics will impact operational parameters of the liquid target. An understanding of bubble behavior is critical for the ability to predict the behavior of the salt solution during operation. It is also important to be able to predict thermal gradients and the circulation in the vessel.

Radiolysis of water has been very well studied and even without dissolved salts and gases in solution, it has been shown that 50 elementary reactions and their rate constants are required to adequately describe radiolysis of water and its subsequent relaxation. Further complications are added by dissolved species (gases and salts), which can react with hydrated

electrons, radicals, intermediates, and molecular species; these reactions affect both the generation rate of hydrogen and hydrogen peroxide and the decomposition of hydrogen peroxide. Hydrogen peroxide can be oxidized to oxygen, reduced to water, or self-destruct into water and oxygen. Another complication is that such high concentrations of solutes will deposit considerable energy in the solution. According to literature data, gas generation due to electron radiolysis is expected to be one-fourth that due to fission fragments [3], but the power density in the solution was varied to make up for the difference in generation rate. The combined bubble dynamic observation with gas-generation measurements using a gas chromatograph was used to establish a correlation between bubble dynamics and time required for establishing the steady-state concentrations and onset of oxygen formation.

This paper describes the experimental setup and an analysis of the experimental data obtained from the irradiation of the solution. The experimental results obtained will be compared with simulations to fine tune computer models; a future report will provide analysis of the data and a comparison with the results of fluid-dynamics modelling.

2. Experimental Setup

In this experiment, we used the electron beam of a linear accelerator to irradiate a solution volume (geometrically similar to a sector of the SHINE annular solution vessel) to study (1) radiolytic-bubble formation, size, and behavior and (2) thermal hydraulics. The design and fabrication of the apparatus has been described elsewhere [4,5]; further details of the apparatus and its operation are also included in this paper. A full report describing the data derived from this experiment can be found elsewhere [6] Figures 1 and 2 are schematics of the “Bubble Experiment” apparatus. Figures 3 and 4 are photographs of the apparatus as set up.

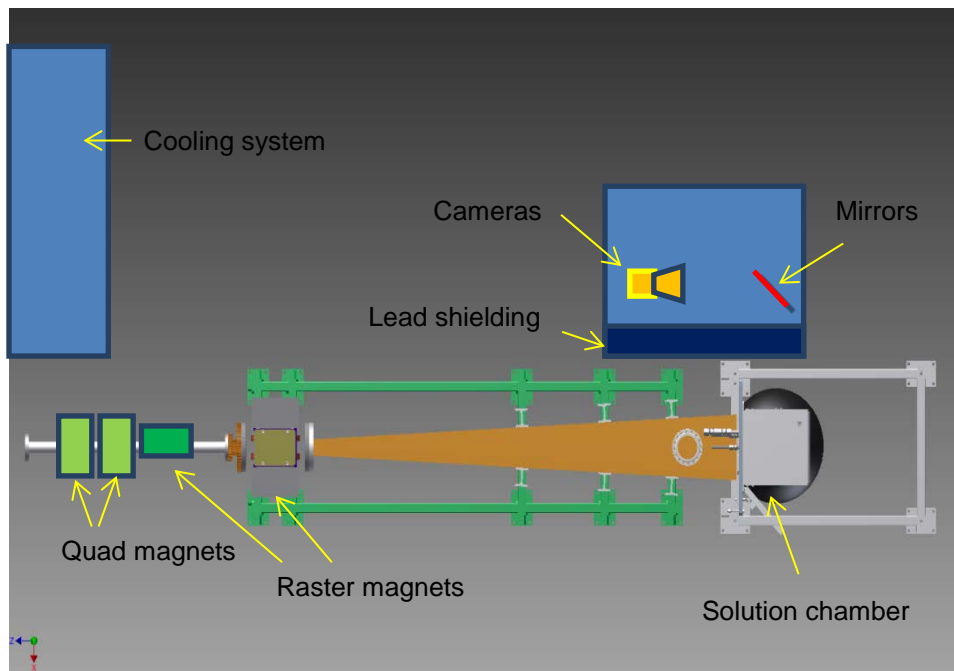


Figure 1. Major elements of the Bubble Experiment apparatus.

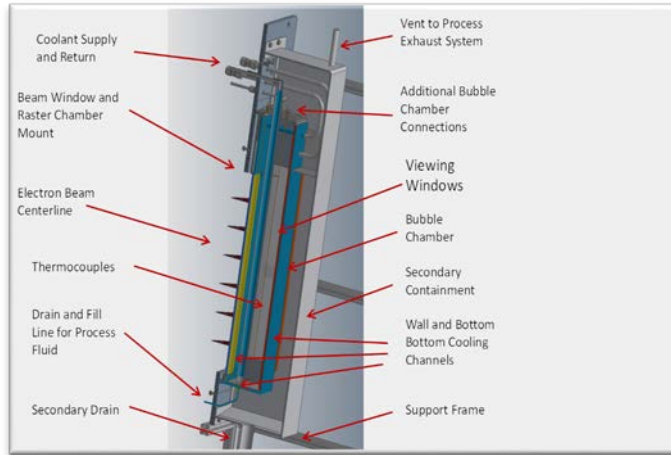


Figure 2. Schematic of the Bubble Experiment apparatus—details of the irradiation vessel.

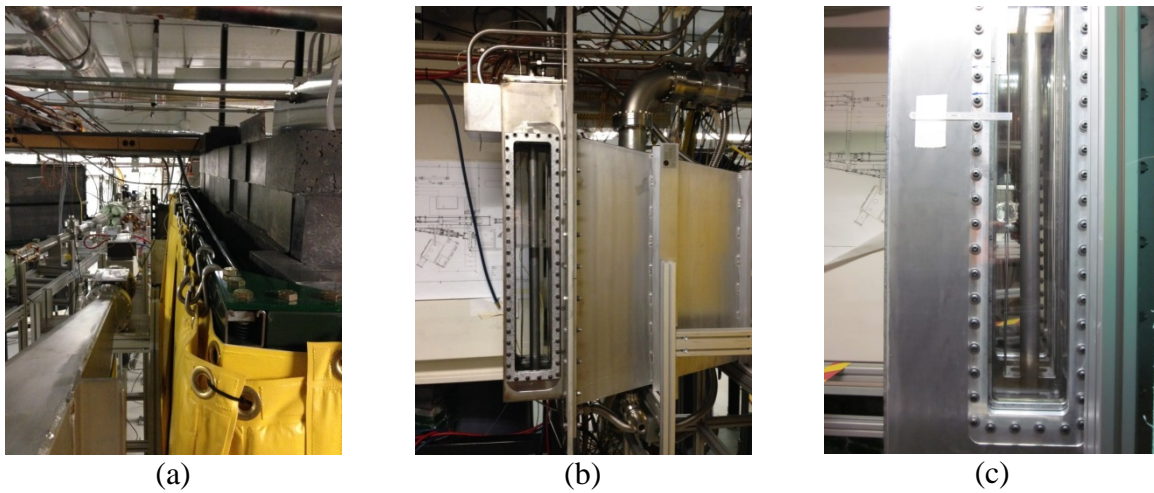


Figure 3. Photographs of the Bubble Chamber experiment showing (a) the linac beamline attached to the raster chamber, (b) the raster chamber attached to the solution vessel primary containment, and (c) a close-up view of the observation window showing the central cooling channel and multi-position thermocouples.

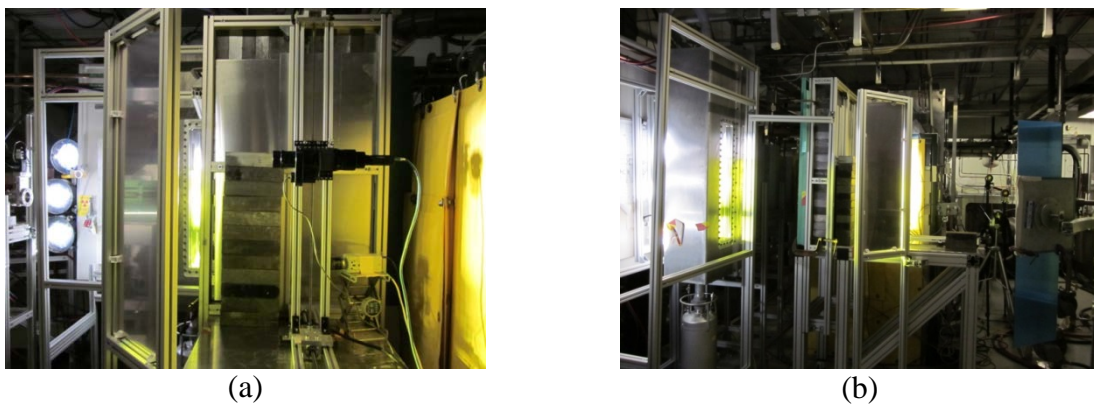


Figure 4. Photographs of the Bubble Chamber experiment with mirrors, backlights and cameras in place. Subfigure (a) is the front view with the electron beam coming in from the right side of the frame and (b) is the view downstream from the incoming electron beam.

Because the solution undergoes radiolytic decomposition from electrons slowing down in the liquid, the study of bubble formation and dynamics and effects of convection and temperature on bubble behavior was possible with this experiment. While data on radiolytic gas formation is being collected in mini-SHINE experiments [7–9], data for bubble-formation dynamics in phase-2 of the mini-SHINE experiments will be limited due to the complexity of the optical setup for the extremely high radiation fields in the fissioning solution. Utilization of the direct electron beam irradiation allows volumetric heating of a large solution volume and simplifies simultaneous observation of the bubble dynamics with thermal-hydraulic data collection.

Irradiations were conducted using a 35 MeV electron beam from a high-power linear accelerator. This electron beam energy translates into 13–17 cm average range of electrons in water, so a large solution volume can be used to study convective behavior resembling the bulk solution. The electron beam was raster-scanned and focused in such a way that almost all of the volume of the 15 cm × 15 cm × 80 cm solution was homogeneously heated. The three electron-beam powers used for this experiment were 6 kW, 12 k, and 15 kW. This power was uniformly distributed in the solution in the direction of the beam due to the low linear energy transfer (LET) of the high energy electrons. The electron beam was scanned over the face of the beam window with 1 Hz frequency to ensure uniform power distribution within the convection time constant of the solution.

The solution volume was actively cooled on the front and back surfaces and by a central tube to mimic the geometry of the proposed SHINE solution vessel. The sides of the irradiation volume were constructed from optical quartz so bubble formation and propagation could be observed using optical cameras. Also, seven six-channel thermocouples were inserted into and above the solution to map its spatially-varying thermal profiles.

Cooling System

The cooling system for the experiment was designed to have sufficient capacity to remove 20 kW of heat. A cooling-water pump was sized to provide 50 gpm of water flow at up to 50 psig pressure. The cooling system had an all-welded design. All components were stainless steel and the system was equipped with a mixed-bed deionizer to remove possible contaminants from the cooling water. The head space of the make-up tank was purged by air and vented through a HEPA-filter-equipped exhaust system to prevent hydrogen buildup. All elements of the cooling system that were not welded were located inside an enclosure to prevent spread of suspect coolant water to the environment.

Beam Handling System

The experimental setup for vessel irradiation requires an even beam deposition over the target surface. To comply with this requirement, a rastering system was designed and installed on the beam line. The concept is to use fast-oscillating low-induction bending magnets so that the beam will cover as much of front target area as possible. To get better uniformity of the power deposition, the beam was defocused in one or both transverse directions. The beam profile forming system consists of two parts: defocusing and rastering as shown in Figure 5.

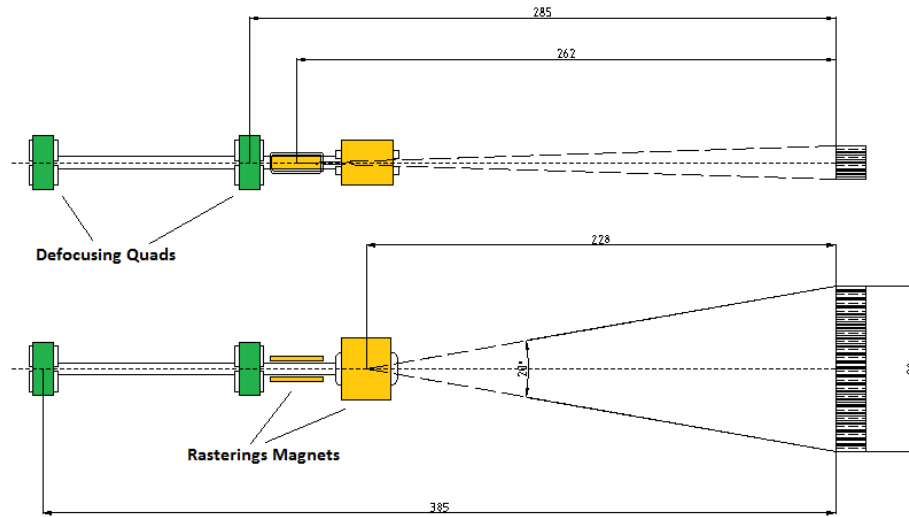


Figure 5. Beam handling system showing the defocusing quadrupole magnets (green) and the rastering magnets (yellow).

Defocusing sub-system: The initial accelerated electron beam has a small transverse size, about 3×5 mm. To increase the beam size in the horizontal and vertical directions, the last quad doublet was used as defocusing elements. This was achieved by over-focusing of the beam in both directions, which increases the spot size on the target to about 30×40 mm. Further defocusing was not applied because this would lead to a dramatic decrease in the beam uniformity and losing of electrons due to energy spread.

Rastering sub-system: The defocused beam was directed to the target front window through the raster system, which consisted of two bending magnets with ability to bend an electron beam in two directions at the $\pm 10^\circ$ in the vertical direction and $\pm 1^\circ$ in the horizontal direction. Their power supplies were controlled by an external programmable pulse forming generator with variable frequency. Two different rastering patterns were tested with the target: first by rastering the beam on the rectangular shape, and second by rastering the beam with “ ∞ ”-shape. Due to its more uniform power-deposition distribution to the target volume (Figure 6), the first pattern was used as the primary operational mode for the experiment.

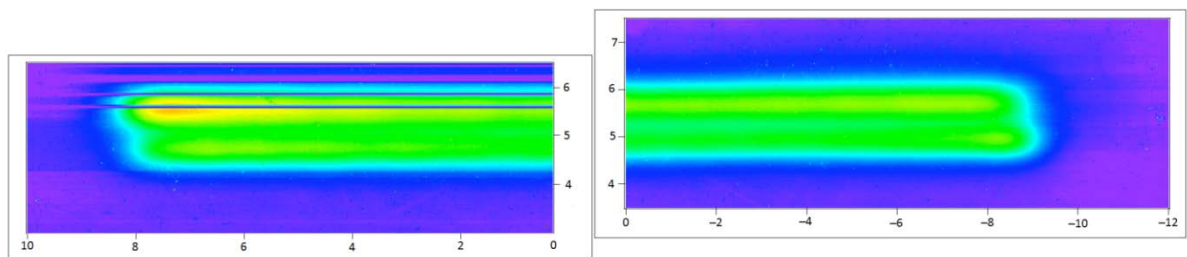


Figure 6. Rectangular beam profile sample obtained from Plexiglas film irradiation. Dimensions are given in inches, the x-axis in this figure is vertical extent of the beam (positive up) and the y-axis is the horizontal extent of the beam from left to right as facing the Bubble Chamber primary.

Temperature Profiling Thermocouples

The solution was instrumented with seven six-channel thermocouples around the central cooling channel, as shown in the Figure 7. Thermocouple channels 1–5 were in the solution

and channel 6 was in the gas head space above the solution. In addition to these thermocouple assemblies, a thermocouple was affixed to the back of the primary containment wall and another was hanging in the secondary containment atmosphere to measure the atmosphere temperature. A LabVIEW-based data-acquisition system was used to collect signals from all thermocouples.

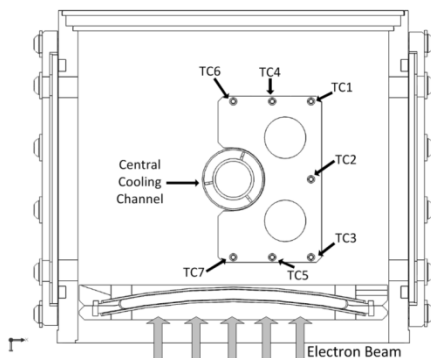


Figure 7. Cross-section of the Bubble Chamber experiment primary containment showing the location of the multi-channel thermocouples.

Camera/Lighting Setup

The task of quantitatively capturing moving sub-millimeter bubbles in solution is non-trivial—when this is to be done in an operating solution reactor with a radiation field requiring a significant standoff distance the challenge is all the more difficult. Thus, careful consideration of lighting, mirrors, lenses, and cameras was taken and based on the best information available regarding the expected characteristics of the bubbles, and preliminary experiments undertaken at the Van de Graaff facility in early FY14 [10], a configuration that could provide the necessary imaging performance was selected. While the size and velocity of the bubbles was not known *a priori*, it was thought to be in the ~1 mm range and having velocities of several cm/s according to the observation of the Micro-bubble experiments at the Van de Graaff facility. Thus, for velocimetry a camera frame rate greater than 100 frames/s was considered necessary. Based on this assumption, a monochromatic camera having a greyscale resolution of 1920×1200 pixels with a global shutter and capable of 162 frames/s enabled by a connection over SuperSpeed USB 3.0 was used (Point Grey Grasshopper model GS3-U3-23S6M-C). This camera was combined with a long-range telecentric lens system from Infinity Photo-Optics USA (K1CentriMax with MX-LR objective, 2 NTX-2× tube adapters, and remote focusing motor) to provide adequate magnification at a stand-off distance of approximately 1.5 m. The lens/camera was mounted on a two-axis traverse stage (controlled by a custom LabVIEW interface) with a linear range of nearly 80 cm to allow access to the entire area of the imaging window. The traverse system was mounted on a custom table, which held a wall of 4” thick lead (for X-ray shielding) and 2” of polyethylene (for neutron shielding) to protect the lens and cameras. A first surface mirror (aluminum on glass) was oriented at 45° in front of the camera to give a precise image of the bubble chamber window with the camera aligned parallel with the beam axis. A second set of mirrors (polished stainless steel) was used to direct the light through the window on the opposite side of the chamber and provide sufficient backlighting for

bubble imaging. Light was provided by a vertical stack of three, 250 W LED stage spotlights (Altman Phoenix Profile LED Spotlight, model PHX2-5600K-10-B).

An additional color camera with higher resolution but lower frame rate (Point Grey Flea model FL3-U3-88S2C-C, 4096×2160, 21 fps, rolling shutter, USB 3.0) was used to view to full length of the chamber window. Given challenges that were encountered in preliminary tests with the stability of the USB 3.0 connection over the long active repeater cables required, an additional set of 3 IP cameras, each a 2 MP VIVOTECK IP7160 connected over Ethernet, was positioned so as to view the top, middle, and bottom of the liquid region of the chamber. IP cameras can record the video continuously over network in 3 gp format through a VAST/ST7501 program installed on a local computer. For better shielding, these four cameras were positioned behind the gas collection system, which already has lead walls against the beam line. Figure 8 shows a diagram of the setup.

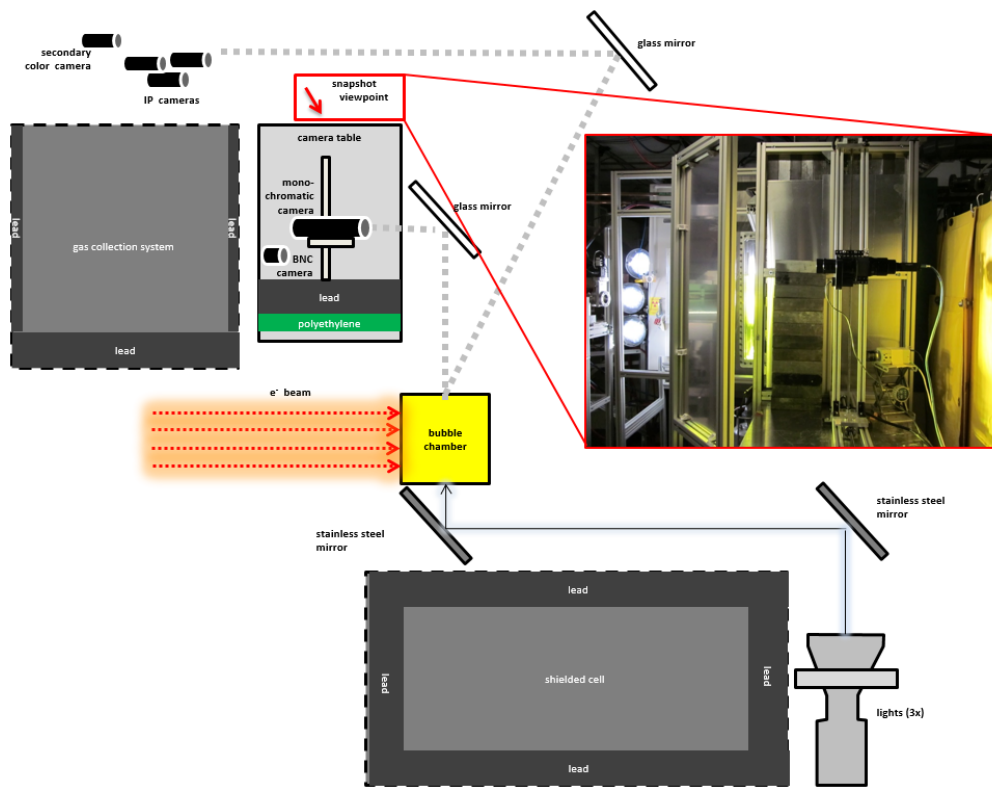


Figure 8. Layout of the imaging setup with the primary bubble imaging camera system mounted behind the wall of lead shielding bricks as shown in the inset snapshot. The viewpoint of the snapshot is shown in the diagram. The mirror on the imaging side is seen in the left foreground and the three 250W LED spotlights can be seen in the background at the left.

While a sufficient number of images were obtained to determine the bubble size and estimate the velocity of the bubbles and bulk liquid, only data at a few points were possible given the delays caused by the instability of the USB 3.0 connection to the cameras. Additionally, quantitative bubble data were obtained only for the 6 kW and 12 kW beam conditions. At the 15 kW power setting, the lens' remote focusing mechanism had become inoperable. The clarity of the final images was also limited due to the necessity of two sets of windows (on the primary and secondary containment) with greater chance for reflection.

3. Results and Discussion

Cooling System Performance

Four thermocouples were installed in the cooling system for the uranyl-sulfate irradiations. These thermocouples were chiller inlet and outlet, pump inlet, and heat exchanger outlet. Two other thermocouples measured ambient temperature and that of the outside body of the apparatus. Cooling-system thermal-performance during the uranyl sulfate irradiation is shown in Figure 9.

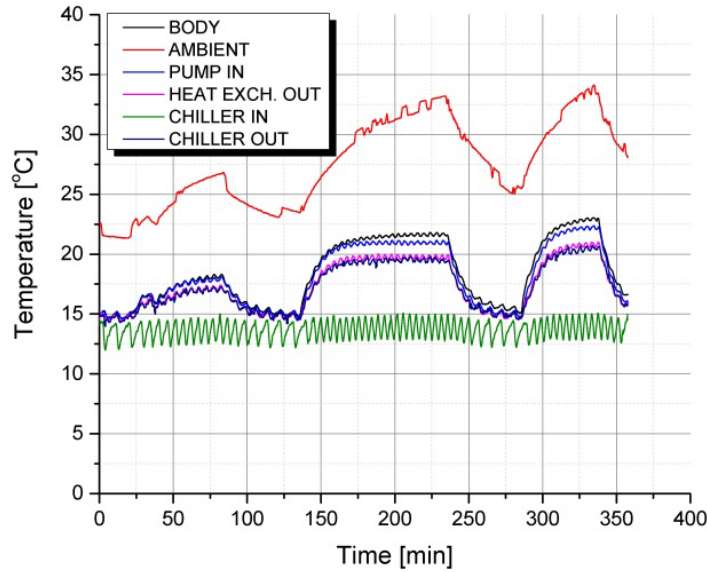


Figure 9. Cooling system performance during the uranyl sulfate irradiation. The peaks correspond to beam powers of 6 kW, 12 kW, and 15 kW.

Based on the collected temperature data, the cooling system performed as designed and expected. The chiller inlet temperature was nearly constant, varying between 13–14°C, while the other five thermocouples tracked thermal loads from the electron beam as various power levels were executed.

Temperature Distribution in the Solution Vessel

Seven thermocouple rods (numbered TC1 through TC7) were inserted in the target solution vessel at various locations; see Figure 7 for the thermocouple layout. There were six measurement points on each rod numbered 1 through 6 starting from the bottom. The first five points were inside the solution, while the sixth one was above the solution in the head space of the target vessel. There were total of 42 temperature measurements—35 inside the target solution and 7 above the solution.

The experiment was performed with a 20 L uranyl sulfate solution (140 g/L of DU). The irradiation of the uranyl sulfate solution was done at 6, 12 and 15 kW of beam power (Figure 10). A maximum steady-state temperature of 70°C was observed at 15 kW of beam power. Roughly 58% of the beam power is deposited in the target solution, which means that at 15 kW the average power density of the target solution is about $15 \times 0.58 / 20 = 0.435$ kW/L.

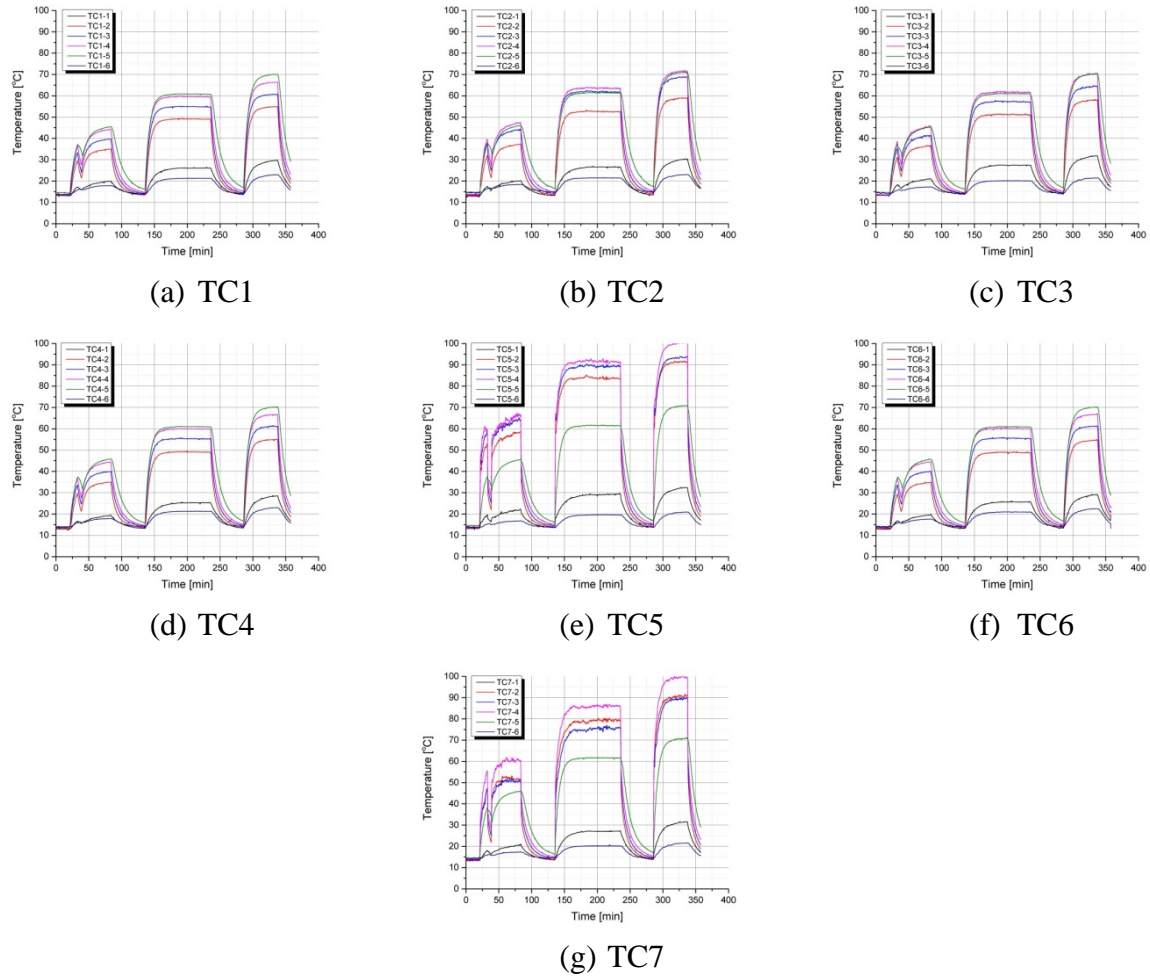


Figure 10. Temperature distribution profiles for each TC set for the irradiation with uranyl sulfate at 6, 12 and 15 kW of beam power. TC5 and TC7 are getting hit directly by the beam.

Bubble Formation and Transport

As described in the previous section, multiple cameras were used simultaneously to qualitatively observe the operation of the experiment and investigate the phenomena of bubble formation and transport during irradiation. Figure 11 shows a composite of representative images from the various cameras for steady-state conditions at 12 kW beam power. Due to the relatively poor resolution and magnification of the other cameras, only the primary camera was sufficient for quantitative image processing of bubble size and velocity. Even then, images of sufficient quality and contrast could only be obtained at several points near the upper liquid surface as well as a couple points at the beam centerline where lighting was adequate.

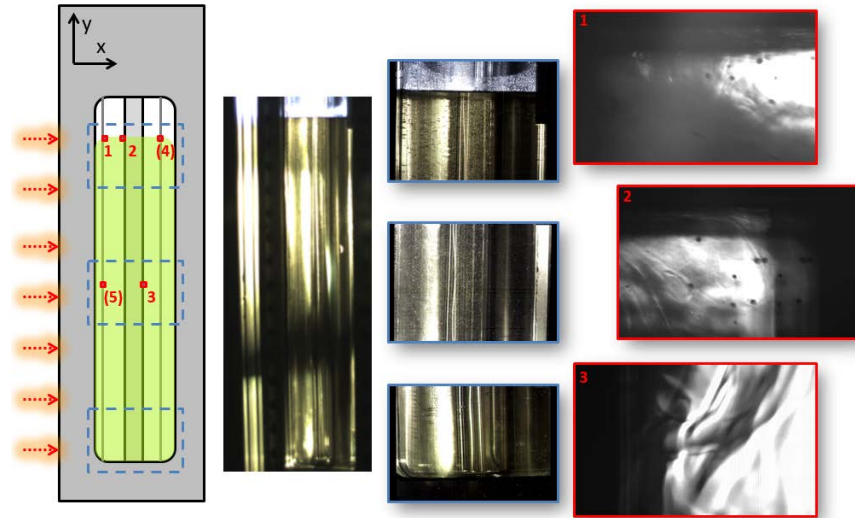


Figure 11. Composite of images from the various cameras showing representative snapshots of the steady-state flow conditions at 12 kW beam power. The images at the far right in which bubbles appear as dark circles are from the primary camera which has a field of view of approximately $13 \text{ mm} \times 8 \text{ mm}$.

In general, it was found that the expected natural circulation loop with the flow going upward near the front surface (relative to the beam direction) and downward at the center cooling channel and beyond. The general flow pattern could be observed by noting refraction fronts due to local density variation similar to the technique use in shadowgraphy (see inset for position 3 in Fig. 11). While such density striations aided in observation of the bulk liquid flow, they unavoidably complicate bubble imaging by distorting bubble shape and focus. Despite this, the bubbles could be easily observed in the high magnification, primary camera images as dark circles. In the secondary cameras, the bubbles appear more as glints of reflected light due to the glancing angle of the camera and mirror orientation in this case. The bubbles appeared to be homogenously nucleated (in the solution as opposed to on surfaces) with the majority of visible bubbles found in the upper half of the domain and virtually none in the lower $\sim 1/3$ of the vessel.

Cherenkov radiation was seen when the electron beam from LINAC hit the target solution (Figure 12 (a), (b)). At the place where Cherenkov radiation was observed, its intensity was much stronger than that of the lighting from three 250 W LED stage spotlights. Since the scanning frequency of the electron beam did not synchronize with the capture speed of the cameras (frame rate), Cherenkov radiation only lit up a small area with a low scanning frequency in the videos captured by the cameras. It may be possible to eliminate the need of external lighting by synchronizing the scanning speed of electron beam with the frame rate of cameras. In the current experimental configuration, lighting from LED stage spot lights are absolutely necessary.

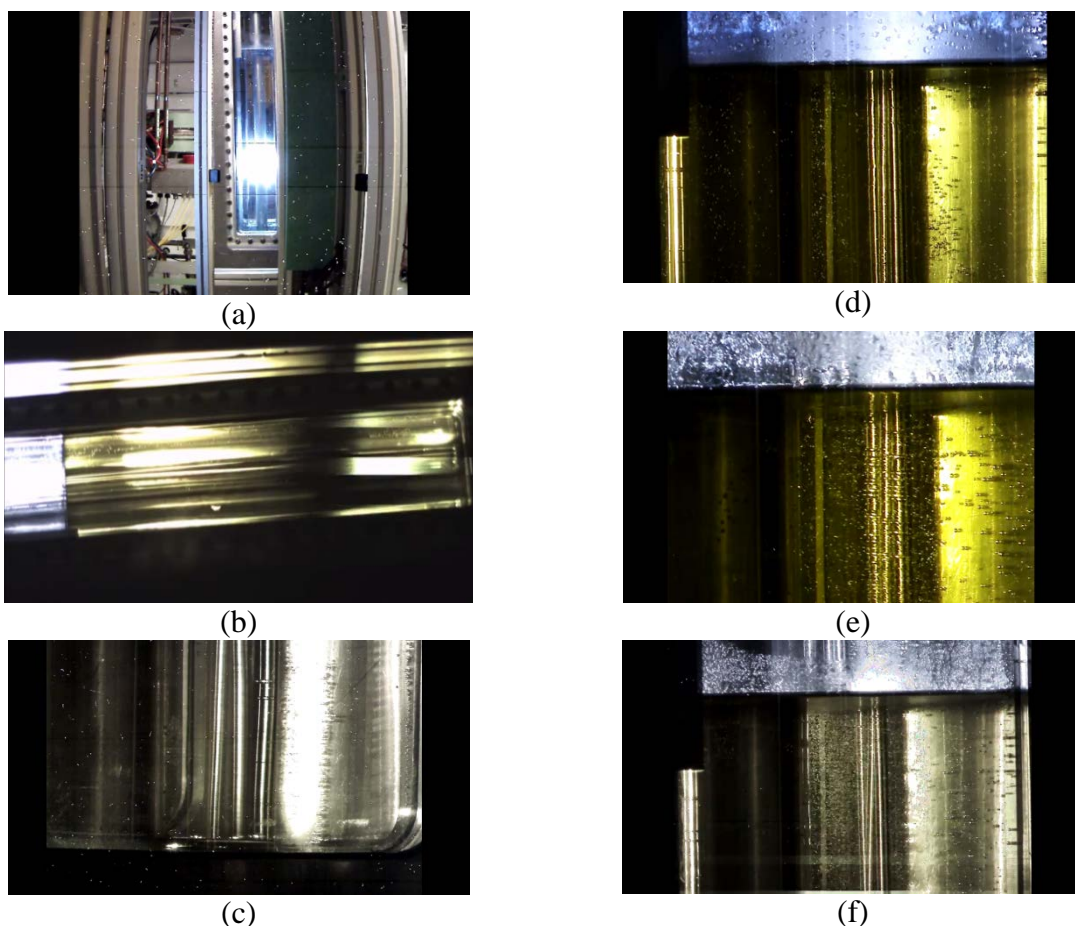


Figure 12. Some video frames captured by the IP cameras: (a) Cherenkov radiation in water test, video was captured by low resolution BNC camera; (b) Cherenkov radiation in uranyl sulfate solution, video was captured by colored USB camera horizontally; (c) bottom view of the solution at 15 kW beam power, two thermal couples were “dancing slowly” with their vibration appeared as a sinusoidal wave; (d) top view of the solution at 6 kW beam power; (e) top view of the solution at 12 kW beam power; and (f) top view of the solution at 15 kW beam power, a thermal couple was “dancing” in the solution.

Large quantities of bubbles were seen in all the irradiations with different incoming beam power (6 kW, 12 kW, and 15 kW). Since (1) the uranyl-sulfate solution headspace was flushed with helium gas for about six hours before the experiments to purge air in the system and (2) the bubbles were created consistently during the long irradiation period, it is conceivable that the bubbles had not come from any air previously in the solution, but originated from the radiolysis of uranyl sulfate instead. The later data analysis from the gas collection system also supports this claim: a significant amount of hydrogen and oxygen were observed in the head space above the bubble chamber. From visual observation of the IP cameras, one can notice that the bubbles started to show up about 1/3 height of the bubble chamber and then rose up to the surface. Bubble coalescence was not seen visually in the middle of the solution, with only a few isolated cases of coalescence observed along the walls of the chamber where some bubbles were adhered. This observation is also confirmed by the sized distributions reported in the next section.

No foam was seen or built up at the surface or inside of the uranyl-sulfate solution (Figure 12 (d), (e), (f)). For all power levels tested and at all times, all the rising bubbles broke and released into the head space. About 5 minutes after the irradiation, the entrained gas was all released from the solution, and the solution returned to clear state. Therefore, it is unlikely that bubble generation should produce any foam that could block any tube and transport lines in the future SHINE plants as had previously been considered a possible concern.

The bubble size in three different powers did not change dramatically. Instead, the number of bubbles increases noticeably according to the beam power. The flow patterns in the 6 kW case were more clearly in a transition to a turbulent regime whereas the higher power cases (12 kW and 15 kW) exhibited more turbulent-like behavior (Figure 12 (d), (e), (f)).

The thermocouple closest to the beam was found to vibrate noticeably, particularly at the 12 kW and 15 kW conditions (Figure 12 (c), (f)). While this vibration appeared as a sinusoidal wave on the IP cameras, this was an artifact of the relatively long exposure time and rolling shutters on these cameras. From the USB 3.0 cameras the motion was more apparent as a single-mode bend vibration over the length of the tube. A set of images from the primary camera were taken at a vertical position at the beam height and focused on the vibrating thermocouple tube (TC position 5) during the 12 kW conditions. Unfortunately, the period of the oscillation could not be clearly determined due to a substantial number of skipped frames in the set, but the magnitude of the vibration at the beam height was found to be approximately 2 mm in the imaging plane.

The advantage of using a telecentric lens system is that focal plane can be scanned in and out in depth with no change in magnification. Thus while the depth of field of the focal plane is rather small, any features that may not be fully in focus are still of the correct size. The ability to scan in the depth also made it possible to gain some qualitative insight into the variation of the flow in the transverse plane. From this effect, it was observed that the majority of bubbles were in the central region of the flow. Further, it was found that just in front of the central cooling channel the flow was in the downward direction near the channel, but flowing upward near the sides window. Unfortunately, there was no internal reference system to determine the actual depth position of focus. Rather, the position of the focal plane was chosen so as to optimize the clarity of features in the flow.

Bubble Size Distribution

Quantitative scaling of the acquired images from the primary camera was done by taking an image of one of the thermocouple tubes with a known diameter of 1/8". The physical scale of the image was thus determined to be 6.7 $\mu\text{m}/\text{pixel}$ making the overall image dimensions 12.9 mm \times 8.0 mm. The ImageJ¹ software was used to identify and measure each individual bubble taking care to not double count a given bubble in multiple frames. Conversely, when the same bubble is measured in successive frames such as is done for velocity estimation as presented in the next section, one can get an estimate of the uncertainty on the diameter measurement. On average, the uncertainty was found to be about $\pm 5\%$. A representative bubble-size distribution for both the 6 kW and 12 kW power levels near the top of the liquid and just inside the center cooling channel (position 2) is shown in Figure 13. In both cases, the bubble size distribution seems to follow a normal distribution, indicating no significant

¹ [Imagej.nih.gov/ij/](http://imagej.nih.gov/ij/)

bubble coalescence is occurring in the system (when a log-normal distribution would be expected) and a dilute regime assumption should be valid.

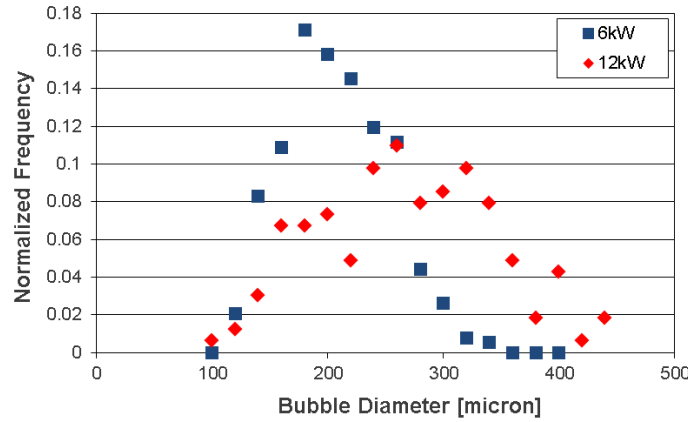


Figure 13. Bubble size distribution near the top of the liquid just inside the center cooling channel (position 2) for the 6 kW and 12 kW power settings.

The mean diameter in all cases is perhaps slightly smaller for the 6 kW condition with an overall mean of 205 μm compared to 267 μm microns for the 12 kW case (Table 1). If one assumes there is some significance to the difference, it is not clear if this is due to the increase the average temperature of the solution or due to the increase gas production rate at the higher power deposition rate. While an estimate of the gas-volume fraction is unfortunately not feasible from these data, it was evident from the overall camera views that the number of bubbles increased somewhat with beam power level. Note that this is unfortunately not directly reflected in the number of bubbles that were counted for each case; rather, the opposite is seen. However, this was merely a result of more optimum lighting conditions in the 6 kW case (perhaps due to less severe thermally-induced density gradients) which gave a larger number of measureable bubbles, particularly at position 4. Due to experimental constraints, this position was only imaged for the 6 kW condition.

Table 1. Summary of mean diameter measured at each position for the two power levels. All units are in μm .

Thermocouple Position	6 kW Beam Power	12 kW Beam Power
1	202 \pm 41	280 \pm 78
2	196 \pm 45	258 \pm 80
3	—	—
4	211 \pm 52	—
d_{avg}	205	267
d_{stdev}	48	80
N_{bubbles}	1454	275

Bubble Velocity

Tracking of individual bubbles for estimation of x- and y-direction velocity components was readily done using the coordinates for the fit circle from successive frames. For estimation of the liquid velocity, only a single component could be determined for regions where the flow had a dominant directionality—such as at the top surface where the flow is almost

completely in the x-direction or near the center cooling channel where the flow is downward. In such cases, the striations due to local density variations caused by temperature fluctuations could be tracked to extract the velocity of the propagating wave front. Velocity estimates were somewhat complicated by the fact that there were often skipped frames though the camera software numbered the frames consecutively regardless and the absolute timestamp of the frame was not retrievably saved to the file's metadata. In most cases, the number of skipped frames could be reliably estimated given that over the short range of the high magnification image (~10 mm) the velocity of a given feature did not vary tremendously and linearity could be assumed. Even so, this introduces some level of uncertainty in the velocity measurements and thus they are given here as estimates only. In each case ~10 features (bubbles or density waves) were tracked over several frames and the results averaged. Table 2 gives a summary of the bubble velocity data, and Table 3 gives a summary of the liquid velocity estimations.

Table 2. Summary of bubble velocity estimates showing magnitude with x and y components in parentheses.

Thermocouple Position	6k W Beam Power	12 kW Beam Power
1	—	4.3±1.3 (1.0, 4.0)
2	—	5.0 ± 1.0 (0.8, 4.9)
3	—	—
4	2.3 ± 0.7 (1.4, 1.8)	—

Table 3. Summary of bulk liquid velocity estimates at the various measurement positions. Relevant velocity component listed in parentheses. Note: 6 kW measurement at position 2 may be unreliable.

Thermocouple Position	6 kW Beam Power	12 kW Beam Power
1 (x)	-	0.8 ± 0.3
2 (x)	5.3 ± 2.4	2.0 ± 0.5
3 (y)	-2.1 ± 0.7	-2.7 ± 0.5
4	-	-

The downflow velocity of the 12 kW case is perhaps slightly greater than that at the lower power indicating somewhat enhanced natural convection. This is consistent with the larger top-to-bottom temperature gradient observed in the temperature profiles with increasing beam power. While downflow on the front side of the center cooling channel was observed in both cases, the descending flow on the backside was clearly more prominent at both power levels observed. The bubble rise velocity near the top of the liquid is in the range of 4-5 cm/s for the 12 kW case and only ~2 cm/s for the 6 kW setting. This is perhaps due to the fact that the smaller bubble size in the 6 kW case also has a more significant horizontal component as it experiences greater drag by the bulk flow which is flowing outward (in direction of beam) along the top surface of the solution. It may also simply be due to local differences in the measurement locations.

It can also be noted from the images and videos that the flow in the low power case is clearly more in the laminar-turbulent transition regime whereas that for the 12 kW (and 15 kW) was clearly more turbulent in nature. This has implications for the heat transfer at the cooling walls and will have an impact on the methods used for CFD modeling.

Gas-Liquid Flow Coupling

While some of the smallest bubbles were seen at times to follow the flow—with a few observed even flowing downward with the descending flow near the cooling channel—the majority of bubbles were found rising to the liquid surface. It is not clear from the data whether the flow of the bubbles enhanced or diminished the natural circulation that developed in the system. Qualitatively, it did appear that there were more bubbles in the front half of the domain (on the beam side) where the flow is predominantly upward. A complicating factor to clear interpretation, however, is that increased bubble presence also leads to increased temperature gradients (due to a decrease in the effective thermal conductivity of the solution), thus compounding any effect on the natural circulation flow magnitude that might be present due to the flow of the bubbles themselves. Insight into this matter could be gained from future multiphase CFD studies in which it is more readily possible to separate the effect of the bubbles' flow from the effect of the thermally induced natural circulation flow patterns.

Gas Chromatography

The experiment comprised of 20 L of uranyl sulfate solution covered by a gas head space filled with helium. In order to prevent the accumulation of hydrogen, the head space was continually purged by a flow of helium gas at a rate of 30 mL/min. Gasses were swept from the headspace of the chamber and passed through a 2 L condenser to reduce water vapor content. The sweep gas then entered a sampling valve on the gas chromatograph. As gas flows through the valve it was periodically sampled for analysis. It is a once-through system which terminates with collection of the sweep gas. The pressure in the system was kept sub-atmospheric between 970 and 980 mBar. Sample analysis was performed using a Shimadzu QP2010 gas chromatograph with a molecular sieve 5A column and thermal conductivity detector (TCD). The detector was calibrated using five-point linear external standard calibrations with $s > 0.99$. Reporting limit of measurements is (a) H₂: 0.050 mole %, (b) N₂: 0.0100 mole %, and (c) O₂: 0.0100 mole %. The percent error of measurements is (a) H₂: 1.9 mole %, (b) N₂: 0.5 mole %, and (c) O₂: 2.6 mole %. Percent relative standard deviation of measurements is (a) H₂: 5.8 mole %, (b) N₂: 8.2 mole %, and (c) O₂: 8.3 mole %. The sampling rate of the GCMS was limited by the oven cool-down cycle of the instrument, which ranged from 9 to 19 minutes with a median sampling time of 11 minutes. Initial measurements were made of the gas stream prior to irradiation. The concentrations of hydrogen, oxygen and nitrogen were monitored. Nitrogen was monitored to account for atmospheric oxygen introduced through leaks in the system. Atmospheric oxygen was subtracted from analytical results based on the measured nitrogen concentration using standard mass fractions of air (75.47% nitrogen and 23.20% oxygen in dry air). Neither the solution nor the headspace was sufficiently purged prior to the start of the experiment so residual atmospheric oxygen and nitrogen was present in the sweep gas stream. The mean solution temperature at the GCMS sample points are shown in Figure 14. The mean solution temperature is used to calculate the molar quantities of gases evolved from solution using the Ideal Gas Law.

Figure 15 shows the percent concentration of hydrogen and oxygen in the helium sweep gas at sampling time. The large headspace, condenser volume and the continuous dilution of the sweep gas are acting to smear the data. Concentrations of gases continually increased even through the solution cool down period between irradiation cycles due to the large mixing

volumes present in the system. Hydrogen concentrations need to reach 0.05% to be detected. First detection of hydrogen is at 137 minutes which is 10 minutes after the beginning of the second irradiation. These were short irradiations so solution chemistry and associated hydrogen and oxygen gas production rates were not allowed to reach a steady state. It would be expected for longer irradiations that hydrogen and oxygen concentrations would reach a steady-state maximum level in this experimental configuration since this is a once-through sweep gas system.

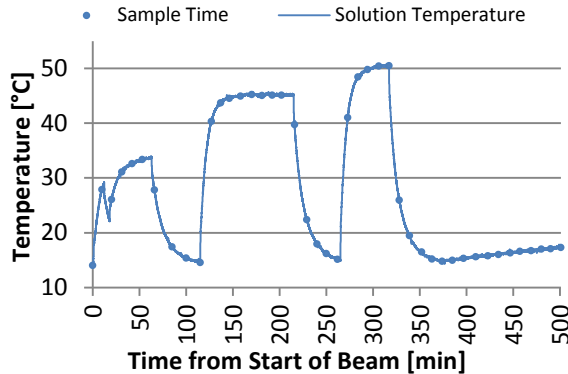


Figure 14. Mean solution temperature at the times GCMS samples were taken.

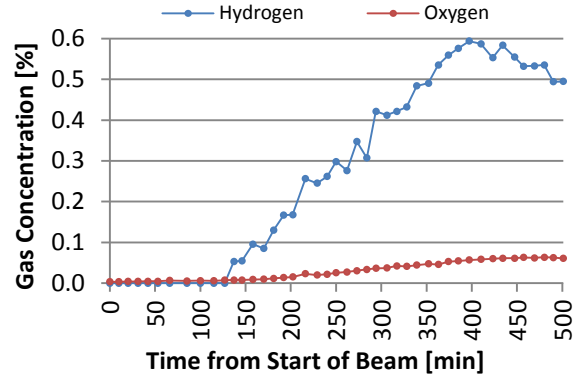


Figure 15. Hydrogen and oxygen molar concentration measured by the GCMS.

Figure 16 shows the μ moles of hydrogen and oxygen swept through the system between sampling times and it follows with Figure 15. Figure 17 shows cumulative hydrogen and oxygen production throughout the experiment at sampling time. A longer irradiation should produce a curve beginning as an exponential function then trending toward a horizontal asymptote as a function of increasing irradiation time.

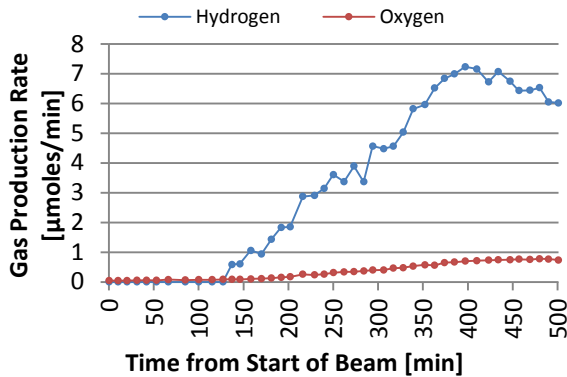


Figure 16. Hydrogen and oxygen production estimates based on sampled gas concentrations.

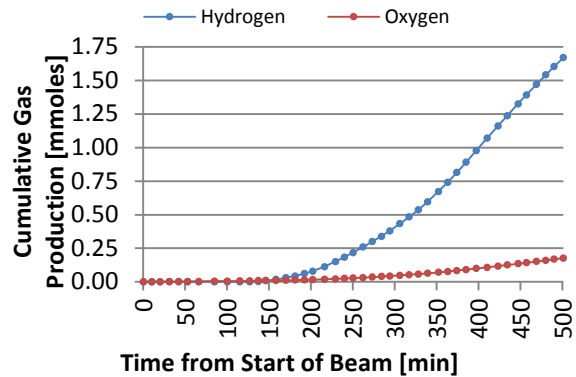


Figure 17. Integrated production quantities of hydrogen and oxygen during the experiment.

Figure 18 is the hydrogen and oxygen ratios both instantaneously at sampling time and cumulatively from the total production to time (t). One would expect the graphs to eventually approach a ratio of 2:1 hydrogen to oxygen as the uranyl sulfate approached the steady-state condition for radiolytic gas production.

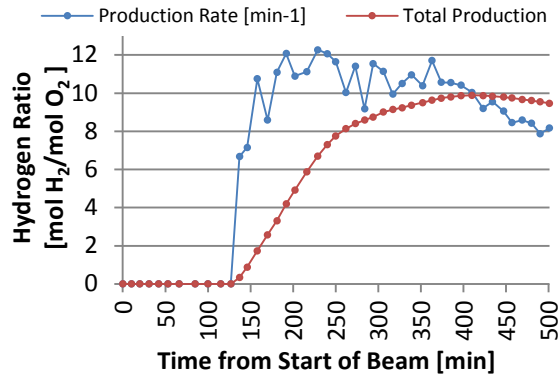


Figure 18. Ratios of hydrogen to oxygen production for sampled concentration and timeintegrated gas production.

Comparison with MCNP6 Calculations

The beam-profile distribution with a rastered beam was measured experimentally after completing the bubble formation study experiments. This was achieved by exposing a Plexiglas sheet with the electron beam for a short period of time (several seconds). The resulting darkened pattern on the sheet was then scanned and the beam distribution profile was obtained. This profile was later incorporated in an MCNP6² model to simulate power deposition distribution in the target solution with a more realistic rastered beam. Electron flux distribution in the XZ plane (beam in traveling along the Y axis in this geometry) just behind the input window was obtained from MCNP6 modeling and is presented in Figure 19. This mimics the electron beam profile of the realistic rastered beam.

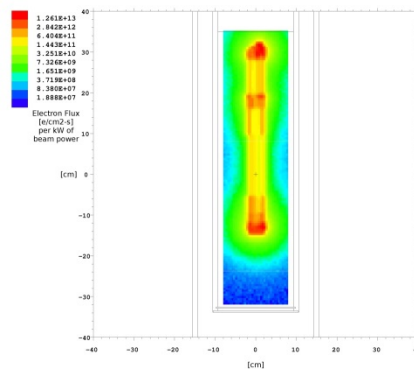


Figure 19. MCNP6 calculated electron flux in XZ plane mimicking the profile of the experimental rastered beam.

Based on this beam profile, 3D total power distributions were obtained from MCNP6 for a 35 MeV electron beam. A 3D mesh with a voxel size of 5 mm × 5 mm × 5 mm was set up over the primary target chamber volume and total power deposition density was tallied for each voxel (type 3 mesh tally). XY, YZ and XZ profiles of this distribution are shown in Figure 20. The units are given in kW/cm³ per kW of incident beam power. According to these results, the peak power density in the solution reaches up to 10 W/cm³ per kW. These

² Monte Carlo N-Particle Transport code

results also show that the power deposition along the beam axis is quite uniform. This is consistent with the observed experimental temperature data.

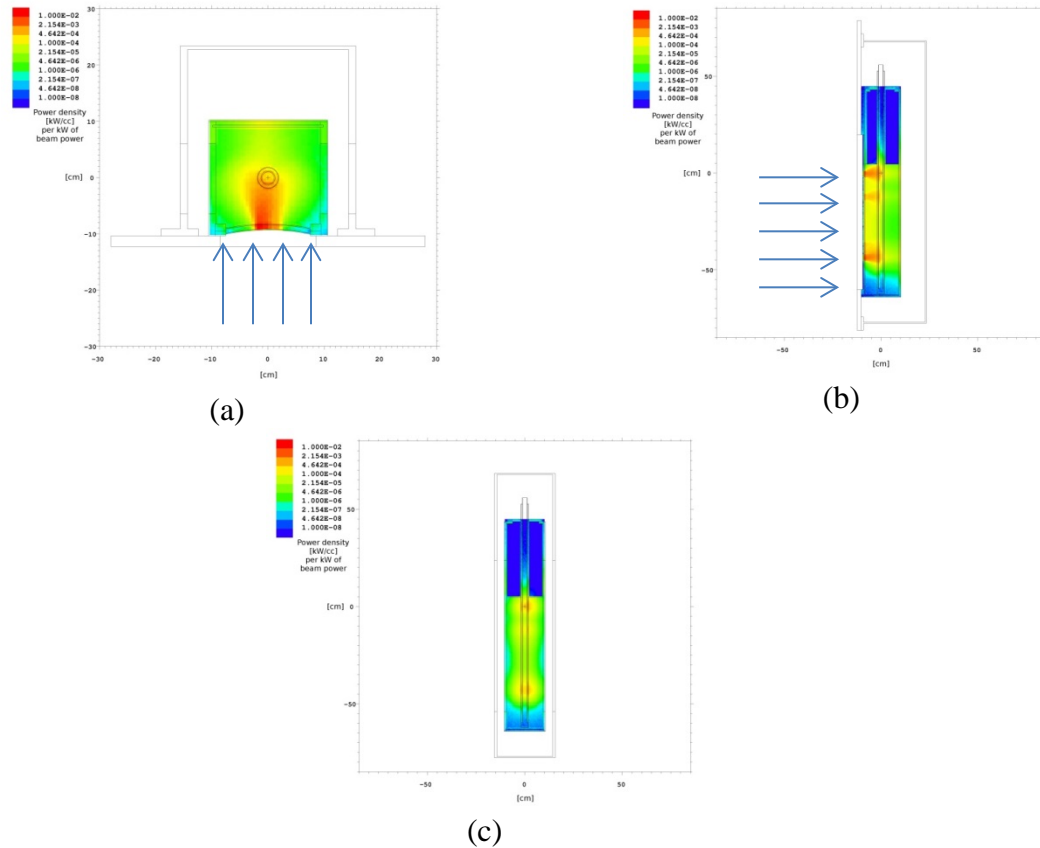


Figure 20. Total power deposition profiles modeled by MCNP6: (a) – XY plane, (b) – YZ plane, (c) – XZ plane. Blue arrows illustrate the beam direction. Units are $[\text{kW}/\text{cm}^3]$ per kW of beam power.

Total powers deposited in each cell of the target geometry were also calculated and are given in Figure 21. The plot shows that about 58% of the beam is deposited in the uranyl sulfate solution. At 15 kW of beam power this amounts to 8.7 kW, which in turn means 0.435 kW/L of average power density. Summing fractional deposited powers over all the cells gives about 86.3% of the initial beam power. The remaining 13.7% is irradiated away by the bremsstrahlung photons.

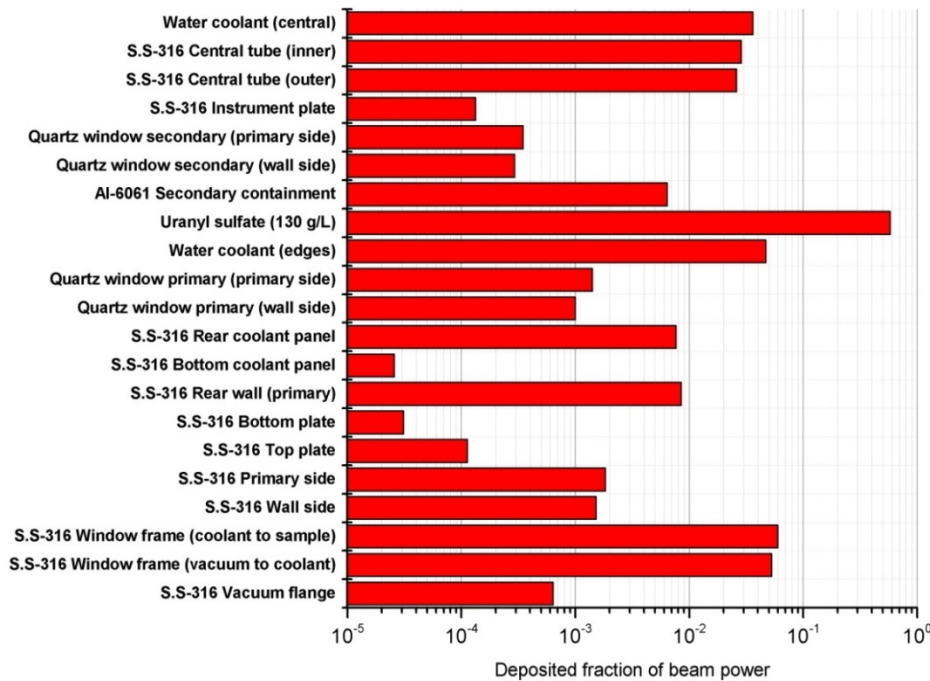


Figure 21. Fractional power depositions in each cell of the target assembly. Modeled with MCNP6 for a 35 MeV rastered beam.

4. Current Work

Initial thermal hydraulic computational fluid dynamic (CFD) analyses were performed on the process fluid in a prototypic bubble chamber in order to determine the temperature distribution in the fluid. The purpose of these analyses was to provide guidance for the design of the cooling system for the bubble chamber. Design criteria for the cooling system were based on the avoidance of boiling in the process fluid. Two independent CFD analyses were performed using different methodologies that resulted in significantly different conclusions. A transient model using more complicated multiphase and turbulence treatment gave a modest temperature rise while a more significant temperature rise was obtained from the steady-state, single-phase model using averaged turbulence. The latter was used for sizing of the cooling system to provide the most conservative value for design purposes. The results of these analyses were described previously [4].

Further thermal hydraulic analyses are required to simulate the actual geometry and experimental conditions and understand the discrepancies between the results in the previous two analyses. Differences in the assumed heat generation distribution, boundary conditions and turbulence models are likely to account for these discrepancies. Also, there is now an opportunity to validate the CFD modeling based on temperature measurements that were taken during the bubble chamber experiment.

We are currently performing a parametric investigation, using the actual bubble chamber geometry including the central cooling channel and applying both CFD analysis methodologies, to determine the sensitivity of the temperature distribution in the fluid to the assumed inputs of heat generation, wall temperatures, bubble characteristics, and turbulence. Evaluation of these results should provide a better understanding of the physical phenomena of importance for accurate prediction that give rise to the differences between the results of the two analyses. Further, based on field measurements taken during the bubble experiment an accurate CFD simulation can be meaningfully compared to the measured temperature distribution in the process fluid. It is anticipated that the result of this analysis work will be a well validated CFD model that will reliably predict the thermal hydraulic performance of the process fluid during irradiation. Such a model will enable additional exploration outside the space covered by the set of experiments (e.g. effect of central cooling channel on overall cooling and potential flow pattern disruption).

5. Conclusions

Although the upcoming CFD analysis of the data will provide a comprehensive set of conclusions, the following conclusions can be reached at this point:

- Bubble formation occurs due to homogenous nucleation in the solution with the majority of bubbles in the upper half of the liquid and virtually none in the lower third.
- The mean bubble sizes found in the systems are quite small—significantly less than 1 mm, in the range of 200–300 μm in all cases—even at the top of the liquid where the bubble size would be expected to be at its largest.
- Bubble size follows a normal distribution indicating no significant coalescence is occurring in the system and a dilute regime assumption should be valid.
- The majority of bubbles rises to the surface and are not recirculated or held up in solution beyond the time it takes for them to rise to the top.
- No foam was seen or built up on the surface or inside of the solution for any conditions tested.
- As the electron beam power increased, the size of bubbles does not increase significantly. However, the number of bubbles increases noticeably.
- Flow patterns in the 6 kW case are more clearly in a transition to turbulence regime, whereas the higher power cases exhibit more turbulent behavior.

6. Acknowledgement

Work supported by the U.S. Department of Energy, National Nuclear Security Administration's (NNSA's) Office of Defense Nuclear Nonproliferation, under Contract DE-AC02-06CH11357. Argonne National Laboratory is operated for the U.S. Department of Energy by UChicago Argonne, LLC.

7. References

- [1] K.M. Pitas, G.R. Piefer, R.V. Bynum, E.N Van Abel, J. Driscoll, T.R. Mackie, and R.F. Radel, “*SHINE: Technology and Progress*,” Proceedings of the Mo-99 2013 Topical Meeting on Molybdenum-99 Technological Development, April 1-5, 2013, Chicago IL.
- [2] Katrina Pitas, “*The SHINE Path to a Reliable Domestic Supply of Mo-99*,” Proceedings of the Mo-99 2014 Topical Meeting on Molybdenum-99 Technological Development, June 24-27, 2014, Washington, DC.
- [3] J.A. Lane, H.G. MacPherson, F. Maslan, “Fluid Fuel Reactors”, 979 pages, Addison-Wesley, 1958, Chapter 3, Properties of Aqueous Fuel Solutions.
- [4] Sergey Chemerisov, Roman Gromov, Vakho Makarashvili, Thad Heltemes, Zaijing Sun, Kent Wardle, James Bailey, Kevin Quigley, Dominique Stepinski, and George Vandegrift, “*Design and Construction of Experiment for Direct Electron Irradiation of a Uranyl Sulfate Solution: Bubble Formation and Thermal Hydraulics Studies*,” ANL/CSE-14/29, Argonne National Laboratory, in press.
- [5] Sergey Chemerisov, Roman Gromov, Vakho Makarashvili, Thad Heltemes, Zaijing Sun, Kent Wardle, James Bailey, Dominique Stepinski and George Vandegrift, “*Experimental setup for direct electron irradiation of the uranyl sulfate solution: bubble formation and thermal hydraulics studies*,” Proceedings of the Mo-99 2014 Topical Meeting on Molybdenum-99 Technological Development, June 24-27, 2014, Washington, DC.
- [6] Sergey Chemerisov, Roman Gromov, Vakho Makarashvili, Thad Heltemes, Zaijing Sun, Kent Wardle, James Bailey, Dominique Stepinski, James Jerden, and George F. Vandegrift, *Experimental Results for Direct Electron Irradiation of a Uranyl Sulfate Solution: Bubble Formation and Thermal Hydraulics Studies*, ANL/NE-15/19, Nuclear Engineering Division, Argonne National Laboratory January 30, 2015, in press.
- [7] S. Chemerisov, A. J. Youker, A. Hebden, N. Smith, P. Tkac, C. D. Jonah, J. Bailey, J. Krebs, V. Makarashvili, B. Micklich, M. Kalensky, S. Zaijing, R. Gromov, and G. F. Vandegrift, “*Development of the Mini-SHINE/MIPS Experiments*,” Proceedings of the Mo-99 2013 Topical Meeting on Molybdenum-99 Technological Development, April 1-5, 2013, Chicago IL.
- [8] A.J. Youker, J.F. Krebs, M. Kalensky, P. Tkac, D. Rotsch, T. Heltemes, D.C. Stepinski, J.P. Byrnes, J.L. Jerden, W.L. Ebert, C. Pereira, M.J. Steindler, D.L. Bowers, S. Zaijing, S.D. Chemerisov, and G.F. Vandegrift, “*Overview: Argonne Assistance in Developing SHINE Production of Mo-99*,” Proceedings of the Mo-99 2014 Topical Meeting on Molybdenum-99 Technological Development, June 24-27, 2014, Washington, DC.
- [9] D.A. Rotsch, A.J. Youker, P. Tkac, D.C. Stepinski, J.F. Krebs, V. Makarashvili, M. Kalensky, Z. Sun, T.A. Heltemes, J.F. Schneider, A.S. Hebden, J.P. Byrnes, L. Hafenrichter, K.A. Wesolowski, S.D. Chemerisov, G.F. Vandegrift, “*Chemical Processing of mini-SHINE Target Solutions for Recovery and Purification of Mo-99*,” Proceedings of the Mo-99 2014 Topical Meeting on Molybdenum-99 Technological Development, June 24-27, 2014, Washington, DC.
- [10] Zaijing Sun, Kent Wardle, Kevin Quigley, Kent Wardle, and Sergey Chemerisov, “*Micro-Bubble Experiments at the Van de Graaff Accelerator*,” September 2014, <http://www.ipd.anl.gov/anlpubs/2015/05/113420.pdf>.

Government License Notice

The submitted manuscript has been created by UChicago Argonne, LLC, Operator of Argonne National Laboratory (“Argonne”). Argonne, a U.S. Department of Energy Office of Science laboratory, is operated under Contract No. DE-AC02-06CH11357. The U.S. Government retains for itself, and others acting on its behalf, a paid-up nonexclusive, irrevocable worldwide license in said article to reproduce, prepare derivative works, distribute copies to the public, and perform publicly and display publicly, by or on behalf of the Government.